HHS Public Access

Author manuscript

J Biomech. Author manuscript; available in PMC 2022 March 05.

Published in final edited form as:

J Biomech. 2021 March 05; 117: 110124. doi:10.1016/j.jbiomech.2020.110124.

Manifold learning based data-driven modeling for soft biological tissues

Qizhi He[1,2], **Devin W. Laurence**[3], **Chung-Hao Lee**[3,4], **Jiun-Shyan Chen**[1]

[1]Department of Structural Engineering, University of California, San Diego, La Jolla, CA 92093, USA

[2]Physical and Computational Sciences Directorate, Pacific Northwest National Laboratory, Richland, WA 99354, USA

[3]Biomechanics and Biomaterials Design Laboratory, School of Aerospace and Mechanical Engineering, The University of Oklahoma, Norman, OK 73019, USA

[4]Institute for Biomedical Engineering, Science and Technology, The University of Oklahoma, Norman, OK 73019, USA

Abstract

Data-driven modeling directly utilizes experimental data with machine learning techniques to predict a material's response without the necessity of using phenomenological constitutive models. Although data-driven modeling presents a promising new approach, it has yet to be extended to the modeling of large-deformation bio-tissues. Herein, we extend our recent local convexity data-driven (LCDD) framework ((He and Chen, 2020) to model the mechanical response of a porcine heart mitral valve posterior leaflet. The predictability of the LCDD framework by using various combinations of biaxial and pure shear training protocols are investigated, and its effectiveness is compared with a full structural phenomenological model modified from Zhang et al. (2016) and a continuum phenomenological Fung-type model (Tong and Fung, 1976). We show that the predictivity of the proposed LCDD nonlinear solver is generally less sensitive to the type of loading protocols (biaxial and pure shear) used in the data set, while more sensitive to the insufficient coverage of the experimental data when compared to the predictivity of the two selected phenomenological models. While no pre-defined functional form in the material model is necessary in LCDD, this study reinstates the importance of having sufficiently rich data coverage in the date-driven and machine learning type of approaches. It is also shown that the proposed LCDD method is an enhancement over the earlier distance-minimization data-driven (DMDD) against noisy data. This study demonstrates that, when sufficient data is available, data-driven computing can be an alternative method for modeling complex biological materials.

For correspondence: Jiun-Shyan Chen, Ph.D., William Prager Chair Professor, Department Structural Engineering, Director, Center for Extreme Events Research, Irwin & Joan Jacobs School of Engineering, University of California, San Diego (UCSD), 441H SME Building, 9500 Gilman Drive, Mail Code 0085, La Jolla, CA 92093-0085, js-chen@ucsd.edu, Tel: 858-534-7034.

Conflicts of Interest

The authors of this paper have no financial or personal relationships with other people or organizations that could inappropriately influence (bias) our work.

Keywords

data-driven material modeling; manifold learning; mitral heart valves; hyperelasticity; local convexity data-driven method

1. Introduction

Constitutive modeling based on the hyperelasticity theory has been a conventional approach for modeling the mechanical responses of soft biological tissues under multiaxial loads for many decades. The seminal work by Fung et al. (1979) provided the foundation for the development of phenomenological constitutive models. These phenomenological models have been used for various applications, such as finite element modeling of the iris (Pant et al., 2018) and cardiac heart valves (May-Newman and Yin, 1998; Prot et al., 2007), where a strain energy density function (SEDF) with a specific functional form is constructed *a priori*. Oftentimes, the specific SEDF with calibrated material constants works well only under certain deformation modes and strain ranges, leading to limited predictivity (see the numerical demonstrations in Sections 3.2-3.4). For example, the improper SEDF yielded physiologically incorrect interpretation in the inverse finite element mitral valve modeling (Lee et al., 2014; Lee et al., 2017).

With significant advances in data science and machine learning technologies, immense progress has been made to establish data-driven computing as an alternative for the conventional constitutive modeling. Data fitting based on neural networks has been explored for engineering materials (Bhattacharjee and Matouš, 2016; Ghaboussi et al., 1991; Ghaboussi et al., 1998; Heider et al., 2020; Liu et al., 2019; Wang and Sun, 2018). Unlike the traditional material identification techniques (Bonnet and Constantinescu, 2005; Madireddy et al., 2015; Mihai and Goriely, 2017; Moussawi et al., 2013) that require a pre-defined constitutive model form, Kirchdoerfer and Ortiz introduced a new data-driven computing paradigm to directly integrate the material identification with modeling procedures, where the material's stress-strain data collected from laboratory experiments are integrated with physics laws in the simulation processes (Kirchdoerfer and Ortiz, 2016; Stainier et al., 2019). When enhanced with machine learning techniques, this data-driven modeling approach could properly capture complex material responses without pre-defined constitutive models provided that sufficient experimental data is available.

Data-driven computing has been applied to linearly elastic materials and dynamic structures (Kirchdoerfer and Ortiz, 2016, 2018), with recent extensions to non-linear elasticity (Ibañez et al., 2017; Ibañez et al., 2018). Moreover, it has been inverted for identification of admissible stress-strain relations from non-homogeneous experimental data (Leygue et al., 2018), which is analogous to inverse finite element modeling. Despite these advances, data-driven methods have not been applied to soft tissue biomechanics, and their effectiveness has yet to be carefully examined by comparing with the conventional constitutive modeling.

The objective of this work is to apply data-driven modeling to soft biological tissues by extending the local convexity data-driven (LCDD) computational framework (He and Chen, 2020) which couples manifold learning with nonlinear elasticity for modeling a

representative mitral valve leaflet's nonlinear anisotropic mechanical responses. Owing to the proposed manifold learning scheme that projects data onto a convex space for dimensional reduction, this method is shown to be robust against noisy data and outliers.

The remaining of this paper is organized as follows. Details of the proposed LCDD modeling framework, the experimental data acquisition and protocols for LCDD training and predictions, and the constitutive models for comparisons with the proposed LCDD method are given in Section 2. In Section 3, the LCDD modeling of a porcine mitral valve posterior leaflet based on biaxial tension and pure shear experimental data are investigated. In this section, three study scenarios, considering different sets of experimental data for model training and predictions, are used to examine the performance of the proposed LCDD method. The effectiveness of the LCDD approach is also compared with the modeling results based on the two phenomenological models. The concluding remarks are provided in Section 4.

2. Methods

2.1 Nonlinear data-driven computational framework

2.1.1 Overview on the theory—The data-driven computational framework can be formulated by the following minimization problem

$$\min_{\hat{\mathbf{z}} \in \mathbb{E}} \min_{\mathbf{z} \in \mathscr{C}} \mathscr{H}(\mathbf{z}, \hat{\mathbf{z}}), \tag{1}$$

where $\mathbf{z}$ and $\hat{\mathbf{z}}$ are the *physical state* (e.g., stresses and strains obtained by physical simulations) and the *measured data* (e.g., stresses and strains from experimental measurements), respectively, $\mathscr{H}$ is a functional to compute the distance between $\mathbf{z}$ and $\hat{\mathbf{z}}$, $\mathbb{E}$ is a set of all measurements collected under different experimental protocols, and $\mathscr{C}$ denotes the dataset satisfying the equilibrium and compatibility condition (i.e., the strain-displacement relation). The standard solution procedures of this data-driven problem are based on fixed-point iterations, where the minimization of $\mathscr{H}$ with respect to $\mathbf{z}$ and $\hat{\mathbf{z}}$ are performed iteratively until the intersection of two datasets in $\mathscr{C}$ and $\mathbb{E}$ is found within a prescribed tolerance (Fig. 1). The minimization corresponding to the physical state is denoted as the *global step*, whereas the one associated with the experimental data as the *local step*.

For modeling biological tissues, the Green strain $\mathbf{E}$ and the second Piola-Kirchhoff (2^{nd} PK) stress $\mathbf{S}$ are considered as the strain and stress measures. The functional $\mathscr{H}$ involves the strain energy-like and complementary energy-like components, expressed as

$$\mathscr{H}(\mathbf{z}, \hat{\mathbf{z}}) = \mathscr{H}((\mathbf{E}, \mathbf{S}), (\widehat{\mathbf{E}}, \widehat{\mathbf{S}})) = \int_{\Omega} d_E^2(\mathbf{E}, \widehat{\mathbf{E}}) + d_S^2(\mathbf{S}, \widehat{\mathbf{S}}) \mathrm{d}\Omega\,, \tag{2}$$

where

$$d_E^2(\mathbf{E},\widehat{\mathbf{E}})=\frac{1}{2}(\mathbf{E}-\widehat{\mathbf{E}}):\mathbf{M}:(\mathbf{E}-\widehat{\mathbf{E}}),\, d_S^2(\mathbf{S},\widehat{\mathbf{S}})=\frac{1}{2}(\mathbf{S},\widehat{\mathbf{S}}):\mathbf{M}^{-1}:(\mathbf{S}-\widehat{\mathbf{S}})\,. \tag{3}$$

Here, **M** is a positive definite coefficient matrix that provides multi-dimensional weights to the distance measure between the experimental stress-strain data $\hat{\mathbf{z}}=(\widehat{\mathbf{E}},\widehat{\mathbf{S}})$ and the physical stress-strain state **z** = (**E,S**). In the numerical studies for nonlinear materials, **M** is defined as a diagonal matrix, in which each diagonal component is the ratio of the standard deviations of the associated components of the stress-strain experimental data. Although being empirical in selecting **M** , this treatment generally yields satisfactory results in our numerical tests in this study.

To consider large deformations in soft tissue materials, we formulate the data-driven computational framework based on the finite strain theory (Belytschko et al., 2013). Given a candidate data $(\widehat{\mathbf{E}},\widehat{\mathbf{S}})$ from the experimental dataset $\mathbb{E}$, the *global step* of the data-driven solver in Eq. (1) is expressed as

$$\min_{\mathbf{u},\,\mathbf{S}}\int_{\Omega^X}[d_E^2(\mathbf{E}(\mathbf{u}),\widehat{\mathbf{E}})+d_S^2(\mathbf{S},\widehat{\mathbf{S}})]\mathrm{d}\Omega\,, \tag{4}$$

$$\text{subject to: } \mathrm{DIV}(\mathbf{F}(\mathbf{u})\cdot\mathbf{S})+\overline{\mathbf{b}}=\mathbf{0}\ \text{in}\ \Omega^X,\ \text{and} \tag{5}$$

$$(\mathbf{F}(\mathbf{u})\cdot\mathbf{S})\cdot\mathbf{N}=\overline{\mathbf{t}}\qquad\text{on}\ \Gamma_t^X\,. \tag{6}$$

Equations (5) and (6) are the equilibrium equation and the associated natural boundary condition, respectively, where **F** is the deformation gradient tensor, $\mathbf{E}=(\mathbf{F}^T\mathbf{F}-\mathbf{I})/2$, **u** is the unknown displacement field, $\overline{\mathbf{b}}$ is the body force at the initial configuration Ω^X, $\overline{\mathbf{t}}$ is the traction on the natural boundary Γ_t^X, and **N** is the surface normal on Γ_t^X. Note that in the displacement-based formulation, **F** and **E** are obtained from **u**, denoted as **F**(**u**) and **E**(**u**). The constrained minimization problem in Eqns. (4)-(6) can be solved numerically using the Lagrange multiplier approach with a standard finite element or reproducing kernel particle method (RKPM, Chen et al. (1996) and Chen et al. (2002)) meshfree numerical solver. The detailed computational formulations are provided in Appendix A.

2.1.2 Computational algorithm for the proposed LCDD nonlinear solver—

The employed data-driven computational method does not rely on any pre-assumed constitutive model for the relationship between **S** and **E**. Instead, it searches for a stress-strain pair $(\widehat{\mathbf{E}},\widehat{\mathbf{S}})$ from the experimental measurement set $\mathbb{E}$ that is closest to the physics strain-stress pair (**E,S**).

In this study, the manifold learning data-driven solver proposed by (He and Chen, 2020) is employed to seek for the solution $\hat{\mathbf{z}}^*=(\widehat{\mathbf{E}}^*,\widehat{\mathbf{S}}^*)$ that minimizes Eq. (1) for a given (**E,S**) obtained from Eqns. (4)-(6). Because the strain-stress pairs $(\mathbf{E}_a,\,\mathbf{S}_a)$ are numerically

computed at the integration points $\mathbf{X}_a$, the minimization of Eq. (1) with the functional in Eq. (2) is reduced to the following minimization problem associated to each integration point $\mathbf{X}_a$

$$(\widehat{\mathbf{E}}_\alpha^*, \widehat{\mathbf{S}}_\alpha^*) = \arg \min_{(\widehat{\mathbf{E}}_\alpha, \widehat{\mathbf{S}}_\alpha) \in \mathscr{E}_\alpha} d_E^2(\mathbf{E}_\alpha \widehat{\mathbf{E}}_\alpha) + d_S^2(\mathbf{S}_\alpha, \widehat{\mathbf{S}}_\alpha),\ \alpha = 1, \cdots, m\,, \tag{7}$$

and thus, called the *local step*. In Eq. (7), $\mathscr{E}_\alpha$ is the material data space reconstructed by the locally-convex manifold associated with $(\mathbf{E}_a, \mathbf{S}_a)$, m is the total number of integration points employed in the solver in Eqns. (A.3)-(A.5). The key idea of the LCDD solver is to construct a locally-convex subset $\mathscr{E}_\alpha$ using k neighboring material data points in $\mathbb{E}$ closest to the given local state $(\mathbf{E}_a, \mathbf{S}_a)$, *called k-nearest neighbors*, and solve Eq. (7) by using the penalty relaxation and non-negative least squares (see Table A1 of Appendix A). In this study, the default value for the number of neighbors is $k = 6$. By imposing suitable smoothness and convexity in the locally-convex manifold, LCDD yields stable data-driven computing results against noisy data and outliers (He and Chen, 2020). Note that when the *raw* experimental dataset $\mathbb{E}$ is directly used for the *local step* in the solver, the standard distance-minimization data-driven (DMDD) method (Kirchdoerfer and Ortiz, 2016) is recovered. More details about constructing the locally-convex data set $\mathscr{E}_\alpha$ by means of manifold learning can be found in He and Chen (2020). The effectiveness of the proposed data-driven computational framework for modeling a transversely isotropic hyperelastic material under uniaxial tension based on the synthetic stress-strain data generated by the Holzapfel model (Holzapfel, 2002) is first verified in Appendix B.

2.2 Application to tissue biomechanics of the heart valve leaflet

2.2.1 Tissue preparation and biaxial mechanical testing—

The biaxial mechanical testing data of one representative porcine mitral valve posterior leaflet (MVPL) tissue was used to evaluate the effectiveness of the proposed LCDD modeling. In brief, one porcine heart obtained from a local slaughterhouse (Country Meat Co., Oklahoma) was cleaned and dissected to retrieve the MVPL. The central 10 × 10 mm section was excised (Fig. 2a). Three thickness measurements were taken via a digital caliper (Westward 1AAU4–0.01mm resolution), and the measurements were averaged to obtain the MVPL tissue's thickness t_{MVPL}. The sample was next mounted to the BioTester system equipped with 1.5N load cells (CellScale, Ontario, Canada) by using four BioRakes delimiting a 7.5×7.5 effective testing region (Fig. 2b). The tissue's circumferential and radial directions were aligned with the BioTester's x- and y-directions. The mounted specimen was submerged in a 37 °C saline bath and characterized using our previously-developed biaxial mechanical testing protocol for the atrioventricular heart valve leaflets (Jett et al., 2018; Laurence et al., 2019; Ross et al., 2019). The biaxial testing consisted of: (i) ten preconditioning cycles of equi-biaxial tensions ($T_{Circ} = T_{Rad} = T_{\max}$), during which a preload of 1% of $T_{\max}$ were applied, to restore the tissue's *in vivo* configuration (Chuong and Fung, 1986), and (ii) ten cycles of 11 different biaxial tension protocols (Table 1). Specifically, there are *nine biaxial tension protocols* (Fig. 2c) and *two pure shear protocols* during which the area is kept constant under combined tension-compression loads (i.e., $\lambda_{Circ}\lambda_{RAD} = 1.0$, Fig. 2d). Here, λ_{Circ} and λ_{Rad} are the circumferential and radial stretches, respectively. Note that the MVPL specimen was loaded at 4.42 N/min to $T_{\max}$ = 100 N/m according to its physiological

condition (Grashow et al., 2006; He et al., 2005; Krishnamurthy et al., 2009). The deformation gradient tensor **F** and the 2nd PK stress tensor **S** were computed by

$$\mathbf{F}=\begin{bmatrix}\lambda_{Circ} & 0\\ 0 & \lambda_{Rad}\end{bmatrix}=\frac{1}{L}\begin{bmatrix}\boldsymbol{u}_x & 0\\ 0 & \boldsymbol{u}_y\end{bmatrix}\text{and }\mathbf{S}=\frac{1}{t_{MVPL}}\mathbf{F}^{-1}diag([T_{Circ},T_{Rad}]), \tag{8}$$

where L = 7.5 mm, and u_x and u_y are the x- and y-displacements, respectively. Note that the shear component of **E** is negligible when using tine-based mounting (Labrosse et al., 2016). The resulting stress-strain data $\hat{\mathbf{z}}=(\widehat{\mathbf{E}},\widehat{\mathbf{S}})=([\hat{E}_{CC},\hat{E}_{RR}],[\hat{S}_{CC},\hat{S}_{RR}])^T$ were used for the subsequent comparative study.

Remark: In data-driving computing for transversely isotropic materials such as the heart valve leaflet, the material orientation should be consistently defined in the material dataset and the simulation model. The material dataset can be rotated "offline" to ensure the alignment of fiber orientations between the specimen and the dataset. In this work, we collected the experimental data and performed the data-driven simulation under the same fixed global coordinates.

2.2.2 Study scenarios to validate the performance of the proposed LCDD method—

Three study scenarios were considered to evaluate the performance of the proposed LCDD method. Two constitutive models (see Section 2.2.3) were also used in these study scenarios as a reference for the proposed LCDD method. Selected biaxial testing protocols from the MVPL data were employed for constructing experimental dataset $\mathbb{E}$, also referred to as model training data, for the LCDD computing and SEDF model parameter calibration, and predictions were made using other protocols that are not considered in the model training data. Note that the simulation results were obtained by using the tissue model's given boundary conditions associated with the testing protocols (Fig. 2e). The root-mean-square deviation normalized with respect to the maximum stress of the data (NRMSD) was used as a measure to assess the predictability of each method.

- **i.** Scenario 1: Protocol 1 for training (single equi-biaxial tension protocol), and Protocols 3 and 5 for predictions to investigate model's performance in extrapolation with limited information provided.
- **ii.** Scenario 2: Protocols 10 and 11 (pure shear protocols) for both model training and predictions to examine model's predictability, considering kinematic states with combined compression and tension.
- **iii.** Scenario 3: Protocols 1, 3, 4, 7, and 8 (mixed biaxial tension and pure shear protocols) for training, and predictions for 2, 5, 6, and 9 to study model's interpolative and extrapolative predictabilities.

2.2.3 Constitutive modeling for comparisons with the LCDD method—

Two constitutive models were used for the study scenarios described in Section 2.2.2. The first is a full structural model modified from Zhang et al. (2016) that does not consider the layer-specific properties

$$\mathbf{S}_{FSM} = \eta_m\left(\mathbf{I} - C_{33}\mathbf{C}^{-1}\right) + \eta_e^{circ}\left(I_{4,circ} - 1\right)^{d_1}\mathbf{N}_{circ} \otimes \mathbf{N}_{circ} + \eta_e^{rad}\left(I_{4,rad} - 1\right)^{d_2}\mathbf{N}_{rad} \otimes \mathbf{N}_{rad} + \eta_c \int_{-\frac{\pi}{2}}^{\frac{\pi}{2}} \Gamma(\theta; \mu_\Gamma, \sigma_\Gamma)\left[\int_0^{E_{ens}(\theta)} \frac{D(x; \mu_D, \sigma_D)}{\sqrt{1+2x}}\left(\frac{1}{\sqrt{1+2x}} - \frac{1}{\sqrt{1+2E_{ens}(\theta)}}\right)\right] \mathbf{N}(\theta) \otimes \mathbf{N}(\theta) d\theta . \quad (9)$$

Herein, η_m, η_e^{circ}, η_e^{rad}, and η_c are the moduli for the non-fibrous ground matrix, circumferentially-aligned elastin fibers (with orientation $\mathbf{N}_{circ} = [\cos 0°, \sin 0°]^T$), radially-aligned elastin fibers (with orientation $\mathbf{N}_{rad} = [\cos 90°, \sin 90°]^T$) and collagen fibers, respectively. $I_4 = \mathbf{N} \cdot (\mathbf{CN})$ is the fourth invariant of the right Cauchy-Green deformation tensor $\mathbf{C} = \mathbf{F}^T\mathbf{F}$, d_1 and d_2 describe the nonlinearity of the elastin fiber response, $\Gamma(\theta; \mu_\Gamma, \sigma_\Gamma)$ is the orientation distribution function with the mean and standard deviation of (μ_Γ, σ_Γ), $E_{ens}(\theta) = \mathbf{N}(\theta)\cdot[\mathbf{EN}(\theta)]$ is the collagen fiber ensemble strain, and $D(x; \mu_D, \sigma_D)$ is the fiber recruitment function with μ_D and σ_D as the mean and standard deviation.

The second model is the Fung-type strain-based model (Tong and Fung, 1976) with the SEDF form

$$W = \frac{c}{2}\left[\exp\left(a_1 E_{CC}^2 + a_2 E_{RR}^2 + 2a_3 E_{CC} E_{RR}\right) - 1\right], \quad (10)$$

where c, a_1, a_2, and a_3 are the model parameters, and E_{CC} and E_{RR} are the circumferential and radial Green strains, respectively (Fig. 2a-b). Note that the shear terms and the higher-order coupling terms could be included in the Fung-type model in Eq. (10) for materials subjected to more profound in-plane shear and with extremely large deformations, such as the one in Sun et al. (2003).

The constitutive model parameters in Eqns. (9)-(10) were obtained by nonlinear least-squares fitting to the acquired biaxial testing data using an in-house differential evolution optimization (DEO) program (Yu et al., 2014). Briefly, n_{pop} uniformly-distributed sets of material parameters were generated, and the residual r_j was computed for each parameter set

$$r_j = \frac{1}{n_{data}}\left[\sum_{i=1}^{n_{data}} \left(S_{CC}^{\exp} - S_{CC,j}^{\text{model}}\right)^2 + \left(S_{RR}^{\exp} - S_{RR,j}^{\text{model}}\right)^2\right]^{1/2}, \; j = 1, \ldots, n_{pop} . \quad (11)$$

Herein, n_{data} is the number of experimental data, the superscript denotes either the experimental data or model prediction, and S_{CC} and S_{RR} are the circumferential and radial 2nd PK stresses, respectively. The residual values and the Euclidian distances associated with the current best parameters were used to update the DEO parameters *exploratively* or *exploitatively*. This iterative optimization was repeated until the residual threshold was reached (max $r_j < 5\times10^{-7}$) or the residual difference between any two consecutive iterations

was negligible ($< 1\times10^{-7}$). The optimal parameters were then used for predictions of other experimental protocols (see Section 2.2.2).

3. Results and Discussion

3.1 Study scenario 1 (single equi-biaxial tension training protocol)

In this study, Protocol 1 was used for training, and Protocols 3 and 5 were used for prediction validation. Both the proposed LCDD method and the chosen two constitutive models yielded excellent fits to the equi-biaxial tension protocol, whereas the DMDD approach was less accurate in capturing the material's *high-tension* responses (Fig. 3a). The predictions for Protocols 3 and 5 (Figs. 3b-c) showed that the performance of the proposed LCDD method is deteriorated as the prediction protocols move beyond the model training range (e.g., NRMSD=0.271 vs. 0.019 for Protocols 5 vs. 1), since insufficient information about the tissue's stress-strain behaviors was used in model training (i.e., only Protocol 1). This trend was shared by the two constitutive models but was less obvious for the full structural model (NRMSD=0.006-0.096) and with similar predictions to the LCDD method for the Fung-type model (NRMSD=0.003-0.265).

3.2 Study scenario 2 (pure shear training protocols)

In the first part of this study, both pure shear protocols (Protocols 10 and 11) were used in model training. The proposed LCDD nonlinear solver yielded better predictions than the DMDD approach (NRMSD=0.013-0.030 vs. NRMSD=0.069-0.103, 1st column of Fig. 4a-b). While both the LCDD and the DMDD approaches could reasonably predict pure shear protocols, the two constitutive models had an apparent difficulty in capturing the compressive behaviors (2nd and 3rd columns of Fig. 4a-b). These results demonstrate the advantage of the data-driven approaches, in which model predictions are not limited by a pre-defined stress-strain relationship and instead rely on the quality and completeness of the experimental data.

In the second part of this study, *when training with only one pure shear protocol and predicting the same pure shear protocol* (Fig. 4c-d), the proposed LCDD method resulted in excellent fits (NRMSD≤0.016), whereas the DMDD is less accurate in capturing the large pure shear deformation (NRMSD>0.093). The DMDD method appears to have relatively inferior predictability for nonlinear, large-deformation bio-tissues, because its search for the measurement data is based on the *closest* Euclidean distance, which presents difficulties for high-dimensional data. In contrast, the proposed LCDD nonlinear solver improves this weakness through a local manifold learning process. For constitutive modeling, the full structural model exhibits a similar behavior of not capturing the compressive deformations, whereas the Fung-type model properly captures both pure shear protocols when trained individually.

3.3 Study scenario 3 (mixed biaxial tension and pure shear training protocols)

In the last comparative study scenario, experimental protocols for training and predictions were selected to test data-driven methods' interpolative and extrapolative prediction abilities, when predictions are *within* or *outside* the ranges of training data with mixed biaxial and

pure shear deformations. The proposed LCDD method provided a good prediction of training data itself (NRMSD=0.019) as well as *interpolative* predictions of Protocols 2 and 6 (NRMSD=0.022; Fig. 5a), but the *extrapolative* predictions were less effective (NRMSD=0.132). The full structural model exhibited an excellent fit to the training data (NRMSD=0.020) as well as the interpolative (NRMSD=0.018) and extrapolative (NRMSD=0.019) predictions when biaxial deformations are considered for both model training and predictions. When the two pure shear protocols (Protocols 10 and 11) together with the biaxial deformation protocols were considered in model training, the LCDD predictions provided similar predictivity to the case without pure shear in training. On the other hand, the full structural model could not capture the compressive deformations due to its pre-defined functional form, and its overall performance was reduced compared to the case without pure shear in model training (Fig. 5b).

These results suggest that a sufficient coverage of deformation range in the training protocols is important to ensure reliable predictions for the LCDD method. The LCDD method with a direct search of experimental data could be more versatile for general deformations as long as the data set is sufficiently rich.

4. Conclusion

In this study, we have applied the LCDD nonlinear solver to modeling biological materials under finite deformations. The goal of the employed data-driven computational method is to solve biomechanics problems governed by conservation laws without using pre-defined material (constitutive) models, but rather, based solely on the experimentally-measured stress-strain data, to offer an alternative approach to the conventional constitutive modeling. A verification problem with synthetic material data was first conducted to validate the effectiveness of the proposed data-driven solver for nonlinear solids. Furthermore, the proposed data-driven method was used to model *a porcine mitral valve posterior leaflet* with the material data collected from biaxial and pure shear mechanical tests. In all the demonstrated verification and validation cases, our proposed LCDD method consistently outperforms the well-established DMDD method. The enhancement is achieved by introducing the local structure (i.e., material manifold) of the dataset via the cluster analysis and the locally convex manifold reconstruction.

The predictability of the LCDD framework by using various combinations of biaxial and pure shear training protocols were investigated, and its effectiveness was compared with a microstructure-informed structural phenomenological model modified from Zhang et al. (2016) and a continuum phenomenological Fung-type model (Tong and Fung, 1976). The LCDD method has comparable performance to the two constitutive models in both model training and *interpolative* predictions, but the LCDD method becomes less effective when the prediction is an extrapolation outside the range of the training data. The effectiveness of LCDD relies on the richness and quality of the data. While the microstructure-informed constitutive model exhibited very good predictivity as calibrated with biaxial tension protocols, it could not properly capture the compressive deformations when the pure shear protocols were incorporated into Study Scenarios 2 and 3. On the other hand, the proposed LCDD nonlinear solver appeared to be minimally affected whenever pure shear data are

used in model training. We showed that the predictivity of the proposed LCDD nonlinear solver is generally less sensitive to the type of loading protocols (biaxial and pure shear) used in the data set, while more sensitive to the insufficient coverage of the experimental data when compared to the predictivity of the two selected phenomenological models.

Constructing a good phenomenological model requires extensive knowledge and experiences in mechanics and materials. Machine learning approaches, on the other hand, were invented to alleviate the extensive requirement of human intelligence by integration with machine learning algorithms and big data, and could ultimately yield new discoveries that have not been discovered before. In the situation when the phenomenological models are not fully representative of the material behaviors, such as the inability to represent the pure shear deformation in the models employed in this study, the data-driven model could offer an alternative approach provided that the method is robust and that the material data is sufficiently rich.

Acknowledgments

Supports from the American Heart Association Scientist Development Grant Award (16SDG27760143) and the Presbyterian Health Foundation Team Science Grant (C5122401) to the 2nd and 3rd author from The University of Oklahoma (OU), and the National Institute of Health under grant number 1 R01 AG056999-01A1 to the 1st and 4th authors from the University of California, San Diego are gratefully acknowledged. CHL (3rd author) was in part supported by the institutional start-up funds from the School of Aerospace and Mechanical Engineering (AME), the IBEST-OUHSC Funding for Interdisciplinary Research, and the research funding through the Faculty Investment Program from the Research Council at OU. DWL (2nd author) was supported by the National Science Foundation Graduate Research Fellowship (NSF GRFP 2019254233).

Appendix

Appendix A. Formulation of the Local Convexity Data-Driven (LCDD) Nonlinear Solver

A.1 The global step of the LCDD method

This section presents the solution procedures of the global step in the proposed LCDD nonlinear solver. The associated constrained minimization problem in Eq. (4) can be transformed into the following functional:

$$\begin{aligned}\mathscr{L}_{DD}(\mathbf{u},\mathbf{S},\boldsymbol{\lambda}) = &\int_{\Omega^X}[d_E^2(\mathbf{E}(\mathbf{u}),\widehat{\mathbf{E}}) + d_S^2(\mathbf{S},\widehat{\mathbf{S}})]d\Omega \\ &+ \int_{\Omega^X}\boldsymbol{\lambda}\cdot[\mathrm{DIV}(\mathbf{F}(\mathbf{u})\cdot\mathbf{S}) - \boldsymbol{\lambda}\overline{\mathbf{b}}]d\Omega - \int_{\Gamma_t^X}\boldsymbol{\lambda}\cdot[(\mathbf{F}(\mathbf{u})\cdot\mathbf{S})\cdot\mathbf{N} - \overline{t}]d\Gamma,\end{aligned} \tag{A.1}$$

where the subscript *DD* denotes the *data-driven* computational framework, $(\widehat{\mathbf{E}},\widehat{\mathbf{S}})$ is the resultant data solution from the previous iteration, $\boldsymbol{\lambda}$ is the Lagrange multiplier in a proper function space. By means of integration by parts and the divergence theorem, we arrived an equivalent form as follows

$$\mathscr{L}_{DD}(\mathbf{u},\mathbf{S},\boldsymbol{\lambda}) = \int_{\Omega^X}[d_E^2(\mathbf{E}(\mathbf{u}),\widehat{\mathbf{E}}) + d_S^2(\mathbf{S},\widehat{\mathbf{S}})]d\Omega - \int_{\Omega^X}[\nabla\boldsymbol{\lambda}:(\mathbf{F}(\mathbf{u})\cdot\mathbf{S}) - \boldsymbol{\lambda}\bar{\mathbf{b}}]d\Omega + \int_{\Gamma_t^X}\boldsymbol{\lambda}\cdot\bar{\mathbf{t}}d\Gamma + \int_{\Gamma_u^X}\boldsymbol{\lambda}\cdot[(\mathbf{F}(\mathbf{u})\cdot\mathbf{S})\cdot\mathbf{N}]d\Gamma\,. \tag{A.2}$$

Following the standard variational approach (Felippa, 1994), we assume $\boldsymbol{\lambda}=\mathbf{0}$ on the essential boundary Γ_u^X and the last term in the above equation can be dropped, which is analogous to the homogeneous boundary condition for the test functions used in the Galerkin approximation. The stationary condition $\delta\mathscr{L}_{DD}(\mathbf{u},\mathbf{S},\boldsymbol{\lambda}) = 0$ with respect to $\mathbf{u}$, $\mathbf{S}$, and $\boldsymbol{\lambda}$ leads to the following three variational equations:

$$\int_{\Omega^X}\delta\mathbf{E}(\mathbf{u}):\mathbf{M}:(\mathbf{E}(\mathbf{u})-\widehat{\mathbf{E}})\mathrm{d}\Omega = \int_{\Omega^X}(\delta\mathbf{F}^T(\mathbf{u})\cdot\nabla\boldsymbol{\lambda}):\mathbf{S}\mathrm{d}\Omega\,, \tag{A.3}$$

$$\int_{\Omega^X}\delta\mathbf{S}:(\mathbf{M}^{-1}:\mathbf{S}-\mathbf{F}^T(\mathbf{u})\cdot\nabla\boldsymbol{\lambda})\mathrm{d}\Omega = \int_{\Omega^X}\delta\mathbf{S}:\mathbf{M}^{-1}:\widehat{\mathbf{S}}\mathrm{d}\Omega,\ \text{and} \tag{A.4}$$

$$\int_{\Omega^X}\delta\nabla\boldsymbol{\lambda}:(\mathbf{F}(\mathbf{u})\cdot\mathbf{S})\mathrm{d}\Omega = \int_{\Omega^X}\delta\boldsymbol{\lambda}\cdot\bar{\mathbf{b}}\mathrm{d}\Omega + \int_{\Gamma_t^X}\delta\boldsymbol{\lambda}\cdot\bar{\mathbf{t}}\mathrm{d}\Gamma := P^{\mathrm{ext}}(\delta\boldsymbol{\lambda})\,. \tag{A.5}$$

From the above formulations, we can see that Eq. (A.3) relates a strain compatibility constraint on the displacement solution $\mathbf{u}$ to strain data $\widehat{\mathbf{E}}$, and $\boldsymbol{\lambda}$ represents the displacement. Similarly, Eq. (A.4) relates the computational stress $\mathbf{S}$ and the measured stress data $\widehat{\mathbf{S}}$. Lastly, Eq. (A.5) is a generalized equilibrium.

Remark: Because the LCDD framework proposed in He and Chen (2020) was developed based on the weak formulation, it can be easily extended to other energy-conjugate strain/stress pairs. For example, the Cauchy stress and its energy conjugate strain (Euler-Almansi strain) or the first Piola-Kirchhoff (1st PK) stress and its energy-conjugate strain (transpose of the deformation gradient) can be used in the LCDD as long as the experimental data expressed in the same stress-strain measures are available. If the asymmetric stress-strain measures are employed in the LCDD framework, such as the 1st PK stress and the deformation gradient, they lead to the increased dimensions in the database and thus is less desirable. The selection of the energy-conjugate 2nd PK stress and Green-Lagrange strain in our study was due to their symmetry properties, the availability of the experimental information, and their reference with respect to the undeformed configuration.

If the stress approximation is constructed by either static condensation at the element level or nodal integration schemes, Equation (A.4) can be further recast into independent element-wise or point-wise systems (He and Chen, 2020):

$$\mathbf{S} = \widehat{\mathbf{S}} + \mathbf{M}:(\mathbf{F}^T(\mathbf{u}) \cdot \nabla\boldsymbol{\lambda}) \ . \tag{A.6}$$

By substituting Eq. (A.6) into Eqns. (A.3) and (A.5) and rearranging the equations, we obtained

$$\begin{aligned} J_{\mathbf{u}} = &\int_{\Omega^X} \delta\mathbf{E}(\mathbf{u}):\mathbf{M}:\mathbf{E}(\mathbf{u})\mathrm{d}\Omega - \int_{\Omega^X} \left(\delta\mathbf{F}^T(\mathbf{u}) \cdot \nabla\boldsymbol{\lambda}\right):\mathbf{M}:\left(\mathbf{F}^T(\mathbf{u}) \cdot \nabla\boldsymbol{\lambda}\right)\mathrm{d}\Omega \\ &- \int_{\Omega^X} \delta\mathbf{E}(\mathbf{u}):\mathbf{M}:\widehat{\mathbf{E}}\mathrm{d}\Omega - \int_{\Omega^X} \left(\delta\mathbf{F}^T(\mathbf{u}) \cdot \nabla\boldsymbol{\lambda}\right):\widehat{\mathbf{S}}\mathrm{d}\Omega = 0 \qquad , \end{aligned} \tag{A.7}$$

and

$$J_{\boldsymbol{\lambda}} = \int_{\Omega^X} (\mathbf{F}^T(\mathbf{u}) \cdot \delta\nabla\boldsymbol{\lambda}):\mathbf{M}:(\mathbf{F}^T(\mathbf{u}) \cdot \nabla\boldsymbol{\lambda})\mathrm{d}\Omega + \int_{\Omega^X} (\mathbf{F}^T(\mathbf{u}) \cdot \delta\nabla\boldsymbol{\lambda}):\widehat{\mathbf{S}}\mathrm{d}\Omega = P^{\mathrm{ext}} \quad (\delta\boldsymbol{\lambda}) \ . \tag{A.8}$$

The weak form system in Eqns. (A.7)-(A.8) needs to be solved by the Newton-Raphson method with respect to $\mathbf{u}$ and $\boldsymbol{\lambda}$.

To numerically solve the above weak form system, in this study the variables $\mathbf{u}$ and $\boldsymbol{\lambda}$ are approximated by the reproduced kernel (RK) shape functions (Chen et al., 1996; Liu et al., 1995) constructed using the linear basis functions and the cubic-B splines kernel function. These node-based RK approximation functions are employed for better numerical performance under large deformation without experiencing mesh distortion difficulties in the conventional mesh-based methods. The 2nd PK stress $\mathbf{S}$ is approximated by indicator functions so that it can be directly related to discrete stress data $\widehat{\mathbf{S}}$ in Eq. (A.6). Furthermore, the stabilized conforming nodal integration (SCNI) (Chen et al., 2002) is employed for the integration of the weak form in Eqns. (A.7)-(A.8). With SCNI framework, variables $\mathbf{u}$, $\boldsymbol{\lambda}$, and the associated $\mathbf{E}(\mathbf{u})$ and $\mathbf{F}(\mathbf{u})$ are computed at the nodal points (instead of integration points), making it very efficient for data-driven computing where local data search are only performed at the nodal points. More details about the employed discretization scheme can be found in He and Chen (2020).

A.2 The local step of the LCDD method

After the Green strain tensor $\mathbf{E}(\mathbf{u})$ and the 2nd PK stress tensor $\mathbf{S}$ are obtained and the weak form system Eqns. (A.7)-(A.8) and Eq. (A.6), respectively, they are then used to update the measurement data solution $(\widehat{\mathbf{E}}, \widehat{\mathbf{S}})$ from the experimental dataset using Eq. (7) via the proposed locally convexity-preserving machine learning algorithm (He and Chen, 2020).

The key procedure is to recast the minimization problem in Eq. (7) with a convex feasible set $\mathscr{C}_\alpha$ associated with $\mathbf{z}_\alpha = (\mathbf{E}_\alpha, \mathbf{S}_\alpha)$ into the following constrained minimization problem for solving the optimal reconstruction weights $\mathbf{w}_\alpha^* \in \mathbb{R}^k$, $\forall \alpha$=1, K, m:

$$\mathbf{w}_\alpha^* = \arg \min_{\mathbf{w} \in \mathbb{R}^k} \|\mathbf{z}_\alpha - \sum_{i \in \mathcal{N}_k(\mathbf{z}_\alpha)} \boldsymbol{w}_i \widehat{\mathbf{z}}_\alpha^i\|_{\mathbf{M}}, \tag{A.9}$$

$$\text{subject to} \sum_{i \in \mathcal{N}_k(\mathbf{z}_\alpha)} \boldsymbol{w}_i = 1 \text{ and } w_i \geq 0 \ . \tag{A.10}$$

Herein, $\widehat{\mathbf{z}}_\alpha^i = (\widehat{\mathbf{E}}_\alpha^i, \widehat{\mathbf{S}}_\alpha^i)$ are the raw data points in the experimental dataset $\mathbb{E}$, and $\mathcal{N}_k(\mathbf{z}_\alpha)$ represents the indices of the k nearest neighboring data points to $\mathbf{z}_\alpha$. A computationally-feasible algorithm based on the Lawson-Hanson method (Lawson and Hanson, 1995) for non-negative least squares problem is introduced to solve Eqns. (A.9)-(A.10). The overall computational procedures of our proposed LCDD nonlinear solver are summarized in Table A1.

Appendix B. The Verification Problem – Uniaxial Tension of An Anisotropic Material

The effectiveness of the proposed data-driven computational framework is verified by modeling a transversely isotropic hyperelastic material under uniaxial tension (Fig. B1a) based on the synthetic stress-strain data generated by the Holzapfel model (Holzapfel et al., 2000).

$$W(I_1, I_3, I_4) = c_1(I_1 - 3) + \frac{k_1}{2k_2}\left[e^{k_2(I_4 - 1)^2} - 1\right] + \beta(J - 1), \tag{B.1}$$

where $J = \det(\mathbf{F}) = \sqrt{I_3}$, $I_k^{'}\mathrm{s}\,(k = 1, 3, 4)$ are the first, third, and fourth invariants of the right Cauchy-Green deformation tensor $\mathbf{C} = \mathbf{F}^T\mathbf{F}$, β is the penalty parameter for enforcing the incompressibility condition, and the model parameters are chosen as c_1 = 10 kPa, k_1 = 2.5 kPa, k_2 = 0.85.

The material database for the data-driven simulation was generated through the constitutive model based on Eq. (B.1). For simplicity, the strain data points $\widehat{\mathbf{E}}^i = \{\hat{E}_{xx}^i, \hat{E}_{yy}^i, \hat{E}_{xy}^i\}$, i = 1, …, p were uniformly selected from a parameter space [−0 .2,1.5]⊗[−0.25, 0.125]⊗[−0.1, 0.1], where the number of data points is $p = 20^3$. Then, the corresponding stress data points $\widehat{\mathbf{S}}^i = \{\hat{S}_{xx}^i, \hat{S}_{yy}^i, \hat{S}_{xy}^i\}$ were computed by using the following hyperelastic stress-strain relationship

$$\widehat{\mathbf{S}} = \frac{\partial W}{\partial \widehat{\mathbf{E}}} = \frac{\partial W}{\partial I_1}\frac{\partial I_1}{\partial \widehat{\mathbf{E}}} + \frac{\partial W}{\partial I_3}\frac{\partial I_3}{\partial \widehat{\mathbf{E}}} + \frac{\partial W}{\partial I_4}\frac{\partial I_4}{\partial \widehat{\mathbf{E}}} = 2c_1\left(\mathbf{I} - C_{33}\mathbf{C}^{-1}\right) + 2k_1(I_4 - 1)e^{k_2(I_4 - 1)^2}\mathbf{N} \otimes \mathbf{N} \ . \tag{B.2}$$

Herein, the penalty parameter $\beta = -c_1 C_{33}$ is the consequence of imposing the plane-stress condition, i.e., the Cauchy stress component σ_{33} = 0 (see more details in Fan and Sacks

(2014) and Lee et al. (2015)), C_{33} is the 3-3 component of **C**, and the fiber orientation **N** is chosen as $[1,0,0]^T$. These strain and stress data points constitute the experimental dataset $\mathbb{E}$.

In this example, a plane-stress uniaxial tensile deformation was modeled using the LCDD method with the above synthetic stress-strain data. The analytical solution to this uniaxial tension problem is

$$\sigma_{xx} = 2\left(\frac{\partial W}{\partial I_1} + \frac{\partial W}{\partial I_4}\right)\lambda^2 + 2\frac{\partial W}{\partial I_1}\lambda^{-1}, \tag{B.3}$$

where σ_{XX} is the normal Cauchy stress component along the x-direction, and λ is the associated stretch ratio. The 2nd PK stress component under uniaxial tension can be computed: $S_{XX} = \lambda^{-2}\sigma_{XX}$.

Note that the constitutive model-based simulation was chosen as *the reference* for the data-driven computations. Specifically, the problem domain was discretized by 17×5 randomly-spaced RKPM nodes. The numerical analysis was carried out using 10 loading steps, and the constitutive model-based reference solution was obtained by using the finite element software ABAQUS (Dassault Systèmes). The displacement result obtained by the proposed LCDD with 6 nearest neighbors in the local convex hall ($k = 6$, see Table A1) agreed well with the finite element reference solution (Fig. B1b). Figure B1c shows the good agreement between the LCDD prediction and the finite element reference solution, as well as the fast convergence of the solution from our LCDD method.

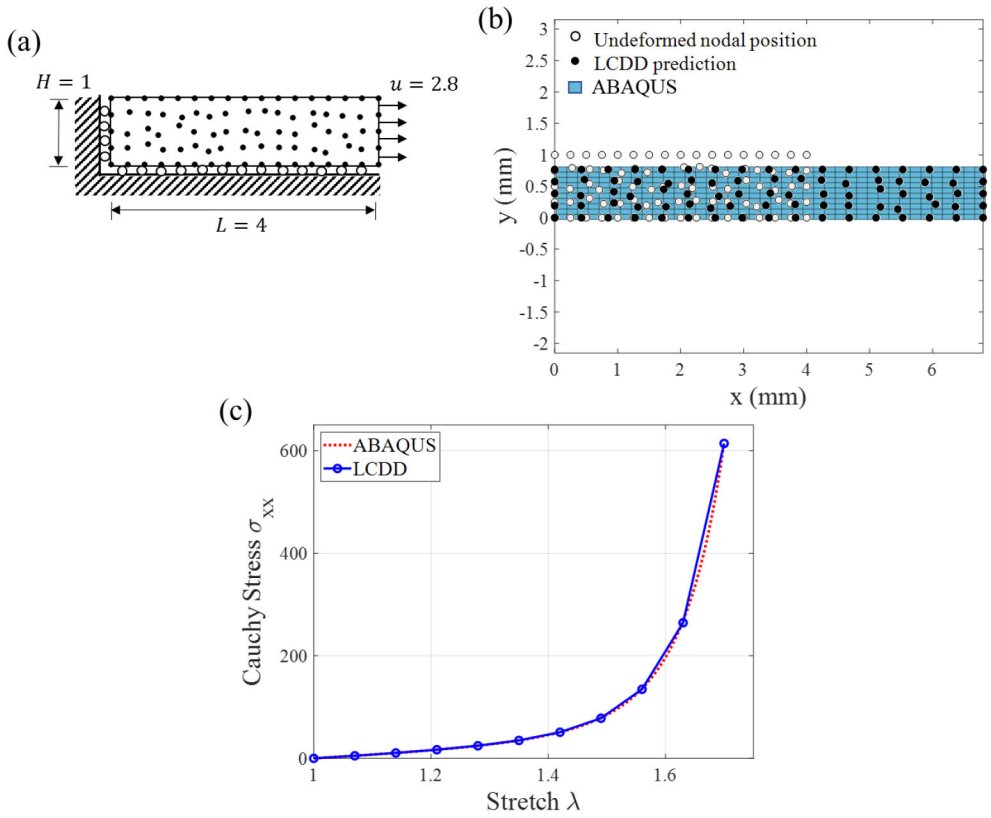

Figure B1.

(a) Schematic of a hyper-elasticity material using the Holzapfel's model in Eq. B.1 subject to uniaxial tension, together with the RK discretization (black circles). (b) Comparison of the ABAQUS finite element reference solution and the RKPM model-based simulation solution. (c) Comparison of the stress vs. stretch relation between the proposed data-driven and the finite element reference solutions.

Table A1.

Computational algorithm of the proposed LCDD nonlinear solver.

Input: Given a measurement data set $\mathbb{E}$, k-nearest neighbor (k-NN) hyper-parameter k, and a convergence tolerance ε

1 **Initialization**. Randomly initialize local data solutions $\widehat{\mathbf{z}}_\alpha^{(0)} = \left(\widehat{\mathbf{E}}_\alpha^{(0)}, \widehat{\mathbf{S}}_\alpha^{(0)}\right) \in \mathbb{E}$, $\alpha = 1,\cdots, m$, and set iteration counter $v = 0$

2 While $\max_{\alpha = 1, \cdots, m} \left\|\widehat{\mathbf{z}}_\alpha^{(v)} - \widehat{\mathbf{z}}_\alpha^{(v-1)}\right\|_{\mathbf{M}} > \mathscr{E}$

Global/Physical Update Step: Input $\left\{\widehat{\mathbf{z}}_\alpha^{(v)}\right\}_{\alpha=1}^{m}$

a. Solve Eqns. (A.7)-(A.8) by the Newton-Raphson scheme for $\mathbf{u}^{(v)}$ and $\boldsymbol{\lambda}^{(v)}$

b. Update computational states $\mathbf{E}^{(v)} = \mathbf{E}(\mathbf{u}^{(v)})$ and $\mathbf{S}^{(v)}$ by Eq. (A.6), and output $\left\{\mathbf{z}_\alpha^{(v)}\right\}_{\alpha=1}^{m} = \left\{\left(\mathbf{E}_\alpha^{(v)}, \mathbf{S}_\alpha^{(v)}\right)\right\}_{\alpha=1}^{m}$

Local/Material Update Step (LCDD solver): Input $\left\{\mathbf{z}_\alpha^{(v)}\right\}_{\alpha=1}^{m}$, for $\alpha = 1,\cdots, m$

c. Select k-NN neighborhood $\mathcal{N}_k\left(\mathbf{z}_\alpha^{(v)}\right)$ for each local state $\mathbf{z}_\alpha^{(v)}$, and assemble those nearest data points $\left\{\widehat{\mathbf{z}}_\alpha^{i}, i \in \mathcal{N}_k\left(\mathbf{z}_\alpha^{(v)}\right)\right\} \subset \mathbb{E}$ into a matrix $\widehat{\mathbf{Z}}_\alpha$

d. The solution of Eq. (7) is given by solving the regularized non-negative least-squares (NNLS) equation below by using a standard active-set NNLS solver (Tropp and Gilbert, 2007; Yaghoobi et al., 2015), and use $\mathbf{w}_\alpha^*$ to output $\widehat{\mathbf{z}}_\alpha^{*(v+1)} = \widehat{\mathbf{Z}}_\alpha \mathbf{w}_\alpha^*$

where $\mathbf{w}_\alpha^* = \arg\min_{\mathbf{w} \in \mathbb{R}^k} \left\| \mathbf{z}_\alpha^{(v)} - \sum_{i \in \mathcal{N}_k\left(\mathbf{z}_\alpha^{(v)}\right)} w_i \widehat{\mathbf{z}}_\alpha^{i} \right\|_{\mathbf{M}}$, subject to $\sum_{i \in \mathcal{N}_k\left(\mathbf{z}_\alpha^{(v)}\right)} w_i = 1$ and $w_i \geq 0$

e. Update $v \leftarrow v + 1$

3 Solution is $\mathbf{z}_\alpha = \left(\mathbf{E}_\alpha, \mathbf{S}_\alpha\right) \leftarrow \mathbf{z}_\alpha^{(v)} = \left(\mathbf{E}_\alpha^{(v)}, \mathbf{S}_\alpha^{(v)}\right)$, $\alpha = 1,\cdots, m$

References

Belytschko T, Liu WK, Moran B, Elkhodary K, 2013. Nonlinear Finite Elements for Continua and Structures. John Wiley & Sons.

Bhattacharjee S, Matouš K, 2016. A nonlinear manifold-based reduced order model for multiscale analysis of heterogeneous hyperelastic materials. J. Comput. Phys 313, 635–653. DOI: 10.1016/j.jcp.2016.01.040.

Bonnet M, Constantinescu A, 2005. Inverse problems in elasticity. Inverse Probl. 21, R1–R50. DOI: 10.1088/0266-5611/21/2/R01.

Chen J-S, Pan C, Wu C-T, Liu WK, 1996. Reproducing kernel particle methods for large deformation analysis of non-linear structures. Comput. Meth. Appl. Mech. Eng 139, 195–227. DOI: 10.1016/S0045-7825(96)01083-3.

Chen JS, Yoon S, Wu CT, 2002. Non-linear version of stabilized conforming nodal integration for Galerkin mesh-free methods. Int. J. Numer. Meth. Eng 53, 2587–2615. DOI: 10.1002/nme.338.

Chuong C-J, Fung Y-C, 1986. Residual Stress in Arteries, in: Schmid-Schnöbein GW, Woo SL-Y, Zweifach BW (Eds.), Frontiers in Biomechanics. Springer-Verlag, New York, pp. 117–129.

Fan R, Sacks MS, 2014. Simulation of planar soft tissues using a structural constitutive model: Finite element implementation and validation. J. Biomech 47, 2043–2054. DOI: 10.1016/j.jbiomech.2014.03.014. [PubMed: 24746842]

Felippa CA, 1994. A survey of parametrized variational principles and applications to computational mechanics. Comput. Meth. Appl. Mech. Eng 113, 109–139. DOI: 10.1016/0045-7825(94)90214-3.

Fung YC, Fronek K, Patitucci P, 1979. Pseudoelasticity of arteries and the choice of its mathematical expression. Am. J. Physiol. Heart Circ. Physiol 237, H620–H631. DOI: 10.1152/ajpheart.1979.237.5.H620.

Ghaboussi J, Garrett J Jr, Wu X, 1991. Knowledge-based modeling of material behavior with neural networks. J. Eng. Mech 117, 132–153. DOI: 10.1061/(ASCE)0733-9399(1991)117:1(132).

Ghaboussi J, Pecknold DA, Zhang M, Haj-Ali RM, 1998. Autoprogressive training of neural network constitutive models. Int. J. Numer. Meth. Eng 42, 105–126. DOI: 10.1002/(SICI)1097-0207(19980515)42:1<105::AID-NME356>3.0.CO;2-V.

Grashow JS, Yoganathan AP, Sacks MS, 2006. Biaixal stress–stretch behavior of the mitral valve anterior leaflet at physiologic strain rates. Ann. Biomed. Eng 34, 315–325. DOI: 10.1007/s10439-005-9027-y. [PubMed: 16450193]

He Q, Chen J-S, 2020. A physics-constrained data-driven approach based on locally convex reconstruction for noisy database. Comput. Meth. Appl. Mech. Eng 363, 112791. DOI: 10.1016/j.cma.2019.112791.

He Z, Ritchie J, Grashow JS, Sacks MS, Yoganathan AP, 2005. *In vitro* dynamic strain behavior of the mitral valve posterior leaflet. J. Biomech. Eng 127, 504–511. DOI: 10.1115/1.1894385. [PubMed: 16060357]

Heider Y, Wang K, Sun W, 2020. SO (3)-invariance of informed-graph-based deep neural network for anisotropic elastoplastic materials. Comput. Meth. Appl. Mech. Eng 363, 112875. DOI: 10.1016/j.cma.2020.112875.

Holzapfel GA, 2002. Nonlinear Solid Mechanics: A Continuum Approach for Engineering Science. Mecc 37, 489–490. DOI: 10.1023/A:1020843529530.

Holzapfel GA, Gasser TC, Ogden RW, 2000. A new constitutive framework for arterial wall mechanics and a comparative study of material models. J. Elast 61, 1–48. DOI: 10.1023/A:1010835316564.

Ibañez R, Abisset-Chavanne E, Aguado JV, Gonzalez D, Cueto E, Chinesta F, 2018. A manifold learning approach to data-driven computational elasticity and inelasticity. Arch. Comput. Meth. Eng 25, 47–57. DOI: 10.1007/s11831-016-9197-9.

Ibañez R, Borzacchiello D, Aguado JV, Abisset-Chavanne E, Cueto E, Ladevèze P, Chinesta F, 2017. Data-driven non-linear elasticity: constitutive manifold construction and problem discretization. Comput. Mech 60, 813–826. DOI: 10.1007/s00466-017-1440-1.

Jett SV, Laurence DW, Kunkel RP, Babu AR, Kramer KE, Baumwart R, Towner RA, Wu Y, Lee C-H, 2018. An investigation of the anisotropic mechanical properties and anatomical structure of porcine atrioventricular heart valves. J. Mech. Behav. Biomed. Mater 87, 155–171. DOI: 10.1016/j.jmbbm.2018.07.024. [PubMed: 30071486]

Kirchdoerfer T, Ortiz M, 2016. Data-driven computational mechanics. Comput. Meth. Appl. Mech. Eng 304, 81–101. DOI: 10.1016/j.cma.2016.02.001.

Kirchdoerfer T, Ortiz M, 2018. Data-driven computing in dynamics. Int. J. Numer. Meth. Eng 113, 1697–1710. DOI: 10.1002/nme.5716.

Krishnamurthy G, Itoh A, Bothe W, Swanson JC, Kuhl E, Karlsson M, Miller DC, Ingels NB Jr, 2009. Stress–strain behavior of mitral valve leaflets in the beating ovine heart. J. Biomech 42, 1909–1916. DOI: 10.1016/j.jbiomech.2009.05.018. [PubMed: 19535081]

Labrosse MR, Jafar R, Ngu J, Boodhwani M, 2016. Planar biaxial testing of heart valve cusp replacement biomaterials: Experiments, theory and material constants. Acta Biomater. 45, 303–320. DOI: 10.1016/j.actbio.2016.08.036. [PubMed: 27570204]

Laurence DW, Ross CJ, Jett SV, Johns CH, Echols AL, Baumwart R, Towner RA, Liao J, Bajona P, Wu Y, Lee C-H, 2019. An investigation of regional variations in the biaxial mechanical properties and stress relaxation behaviors of porcine atrioventricular heart valve leaflets. J. Biomech 83, 16–27. DOI: 10.1016/j.jbiomech.2018.11.015. [PubMed: 30497683]

Lawson CL, Hanson RJ, 1995. Solving Least Squares Problems. SIAM.

Lee C-H, Amini R, Gorman RC, Gorman JH 3rd, Sacks MS, 2014. An inverse modeling approach for stress estimation in mitral valve anterior leaflet valvuloplasty for in-vivo valvular biomaterial assessment. J. Biomech 47, 2055–2063. DOI: 10.1016/j.jbiomech.2013.10.058. [PubMed: 24275434]

Lee C-H, Rabbah J-P, Yoganathan AP, Gorman RC, Gorman JH 3rd, Sacks MS, 2015. On the effects of leaflet microstructure and constitutive model on the closing behavior of the mitral valve. Biomech. Model. Mechanobiol 14, 1281–1302. DOI: 10.1007/s10237-015-0674-0. [PubMed: 25947879]

Lee C-H, Zhang W, Feaver K, Gorman RC, Gorman JH 3rd, Sacks MS, 2017. On the *in vivo* function of the mitral heart valve leaflet: Insights into tissue–interstitial cell biomechanical coupling. Biomech. Model. Mechanobiol 16, 1613–1632. DOI: 10.1007/s10237-017-0908-4. [PubMed: 28429161]

Leygue A, Coret M, Réthoré J, Stainier L, Verron E, 2018. Data-based derivation of material response. Comput. Meth. Appl. Mech. Eng 331, 184–196. DOI: 10.1016/j.cma.2017.11.013.

Liu WK, Jun S, Zhang YF, 1995. Reproducing kernel particle methods. Int. J. Numer. Methods Fluids 20, 1081–1106. DOI: 10.1002/fld.1650200824.

Liu Z, Wu C, Koishi M, 2019. A deep material network for multiscale topology learning and accelerated nonlinear modeling of heterogeneous materials. Comput. Meth. Appl. Mech. Eng 345, 1138–1168. DOI: 10.1016/j.cma.2018.09.020.

Madireddy S, Sista B, Vemaganti K, 2015. A Bayesian approach to selecting hyperelastic constitutive models of soft tissue. Comput. Meth. Appl. Mech. Eng 291, 102–122. DOI: 10.1016/j.cma.2015.03.012.

May-Newman K, Yin FC, 1998. A constitutive law for mitral valve tissue. J. Biomech. Eng 120, 38–47. DOI: 10.1115/1.2834305. [PubMed: 9675679]

Mihai LA, Goriely A, 2017. How to characterize a nonlinear elastic material? A review on nonlinear constitutive parameters in isotropic finite elasticity. Proceedings of the Royal Society A: Mathematical, Physical and Engineering Sciences 473, 20170607. DOI: 10.1098/rspa.2017.0607.

Moussawi A, Lubineau G, Florentin E, Blaysat B, 2013. The constitutive compatibility method for identification of material parameters based on full-field measurements. Comput. Meth. Appl. Mech. Eng 265, 1–14. DOI: 10.1016/j.cma.2013.06.003.

Pant AD, Dorairaj SK, Amini R, 2018. Appropriate objective functions for quantifying iris mechanical properties using inverse finite element modeling. J. Biomech. Eng 140, 074502. DOI: 10.1115/1.4039679.

Prot V, Skallerud B, Holzapfel GA, 2007. Transversely isotropic membrane shells with application to mitral valve mechanics. Constitutive modelling and finite element implementation. Int. J. Numer. Meth. Eng 71, 987–1008. DOI: 10.1002/nme.1983.

Ross CJ, Laurence DW, Wu Y, Lee C-H, 2019. Biaxial mechanical characterizations of atrioventricular heart valves. J. Vis. Exp 146, e59170. DOI: 10.3791/59170.

Stainier L, Leygue A, Ortiz M, 2019. Model-free data-driven methods in mechanics: Material data identification and solvers. Comput. Mech 64, 381–393. DOI: 10.1007/s00466-019-01731-1.

Sun W, Sacks MS, Sellaro TL, Slaughter WS, Scott MJ, 2003. Biaxial mechanical response of bioprosthetic heart valve biomaterials to high in-plane shear. J. Biomech. Eng 125, 372–380. [PubMed: 12929242]

Tong P, Fung Y-C, 1976. The stress-strain relationship for the skin. J. Biomech 9, 649–657. DOI: 10.1016/0021-9290(76)90107-X. [PubMed: 965417]

Tropp JA, Gilbert AC, 2007. Signal recovery from random measurements via orthogonal matching pursuit. IEEE Trans. Inf Theory 53, 4655–4666. DOI: 10.1109/TIT.2007.909108.

Wang K, Sun W, 2018. A multiscale multi-permeability poroplasticity model linked by recursive homogenizations and deep learning. Comput. Meth. Appl. Mech. Eng 334, 337–380. DOI: 10.1016/j.cma.2018.01.036.

Yaghoobi M, Wu D, Davies ME, 2015. Fast non-negative orthogonal matching pursuit. ISPL 22, 1229–1233. DOI: 10.1109/LSP.2015.2393637.

Yu W-J, Shen M, Chen W-N, Zhan Z-H, Gong Y-J, Lin Y, Liu O, Zhang J, 2014. Differential evolution with two-level parameter adaptation. IEEE Trans. Cybernetics 44, 1080–1099. DOI: 10.1109/TCYB.2013.2279211.

Zhang W, Ayoub S, Liao J, Sacks MS, 2016. A meso-scale layer-specific structural constitutive model of the mitral heart valve leaflets. Acta Biomater. 32, 238–255. DOI: 10.1016/j.actbio.2015.12.001. [PubMed: 26712602]

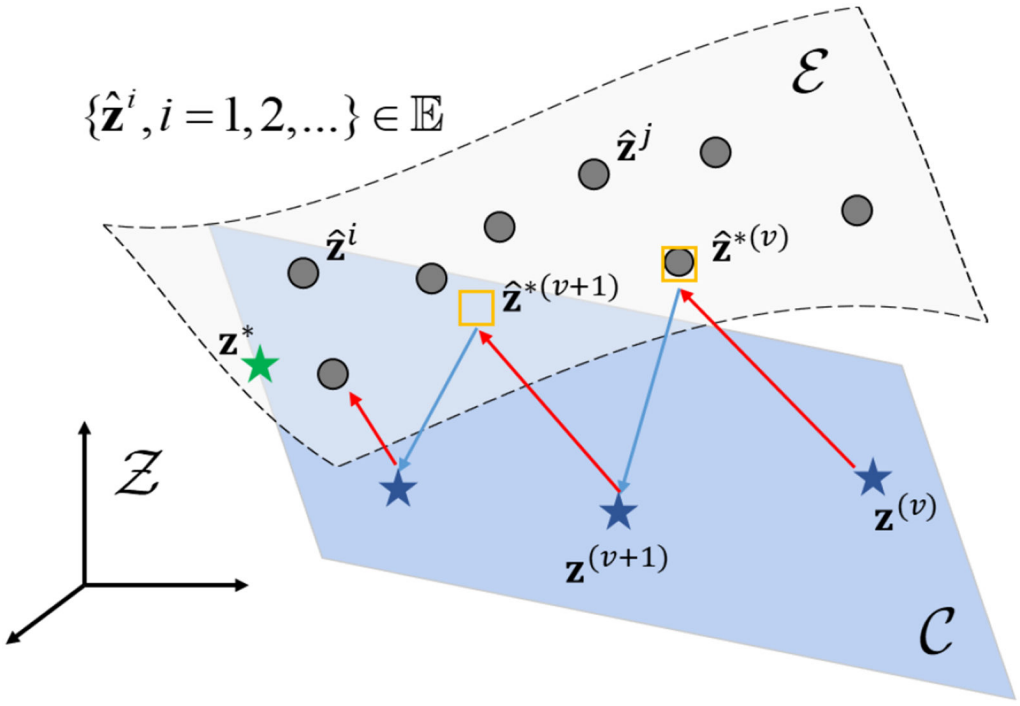

Figure 1.

Geometric schematic of the proposed local convexity data-driven computational framework in Eq. (1) solved by an iteration scheme (with v the iteration counter) where $\mathbf{z}^{(v)} \in \mathscr{C}$ (denoted by the blue stars) is the computation state on the physical manifold $\mathscr{C}$ at v-th iteration, $\{\hat{\mathbf{z}}^i, i = 1, 2, \ldots\}$ (denoted by the gray circles) are the collected measurement data stored in $\mathbb{E}$, $\mathscr{E}$ is an underlying material manifold (or envelope) constructed based on the data, and $\mathscr{Z}$ denote the global phase space. The iteration scheme is decomposed into two update steps (see more details in Table A1): (i) the *local (material) step* where the data solution $\hat{\mathbf{z}}^*$ (denoted by the orange squares) is solved by projecting the given computational state onto the manifold $\mathscr{E}$ of data set and (ii) the *global (physical) step* where the new computational state is obtained by projecting the given data solution onto $\mathscr{C}$ by enforcing the physical constraints. The convergent solution is denoted by $\mathbf{z}^*$ (the green stars), which ideally is $\mathscr{C} \cap \mathscr{E}$.

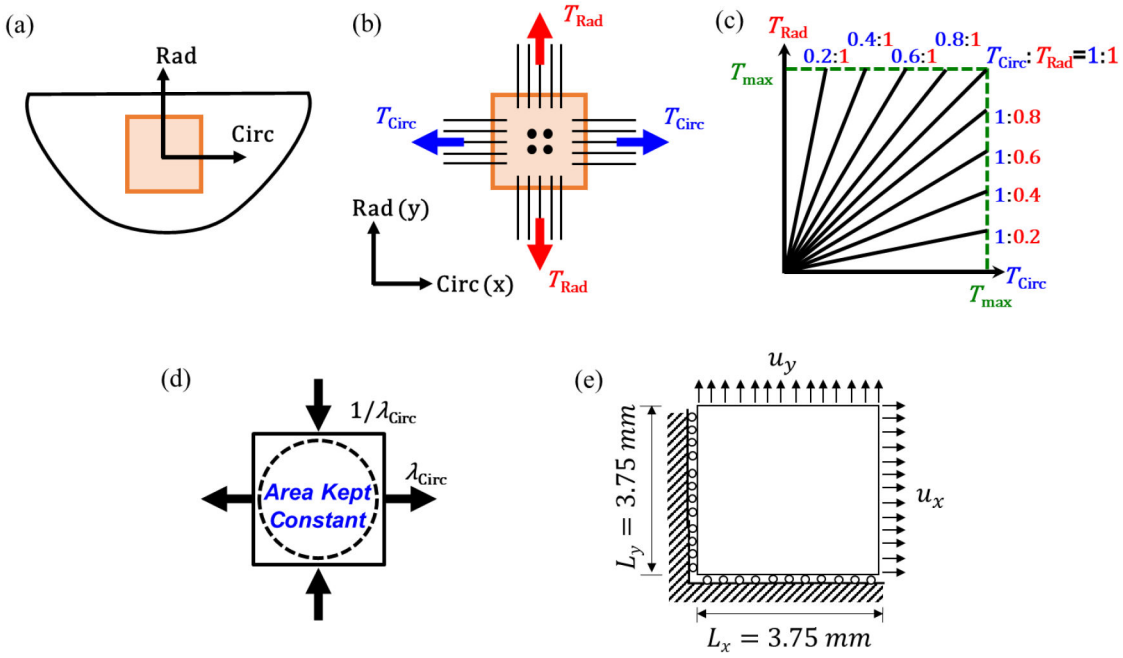

Figure 2.

(a) Schematic of a mitral valve posterior leaflet (MVPL) tissue with the central (belly) region highlighted in orange, and (b) tissue specimen mounted to a biaxial testing system with applied tensions T_{Circ} and T_{Rad}. Schematic of the mechanical testing protocols: (c) biaxial tensions, and (d) pure shear. (e) Schematic of the model of biaxial testing used in data-driven computations and constitutive modeling.

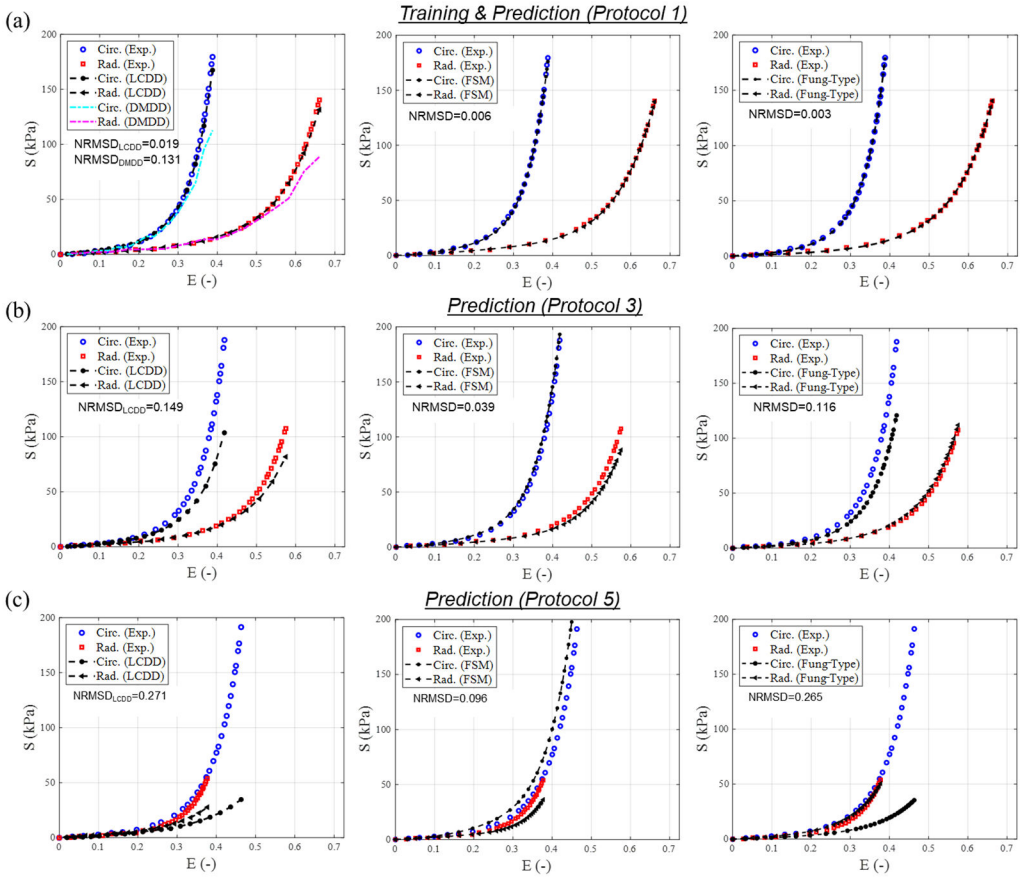

Figure 3.

Comparison of the training and prediction accuracies among the proposed LCDD nonlinear solver, the DMDD solver, and the constitutive models with the Fung-type SEDF and the modified full structural model : (a) training of the equi-biaxial tension data (Protocol 1) together with its prediction, (b) prediction of Protocol 3, and (c) prediction of Protocol 5.

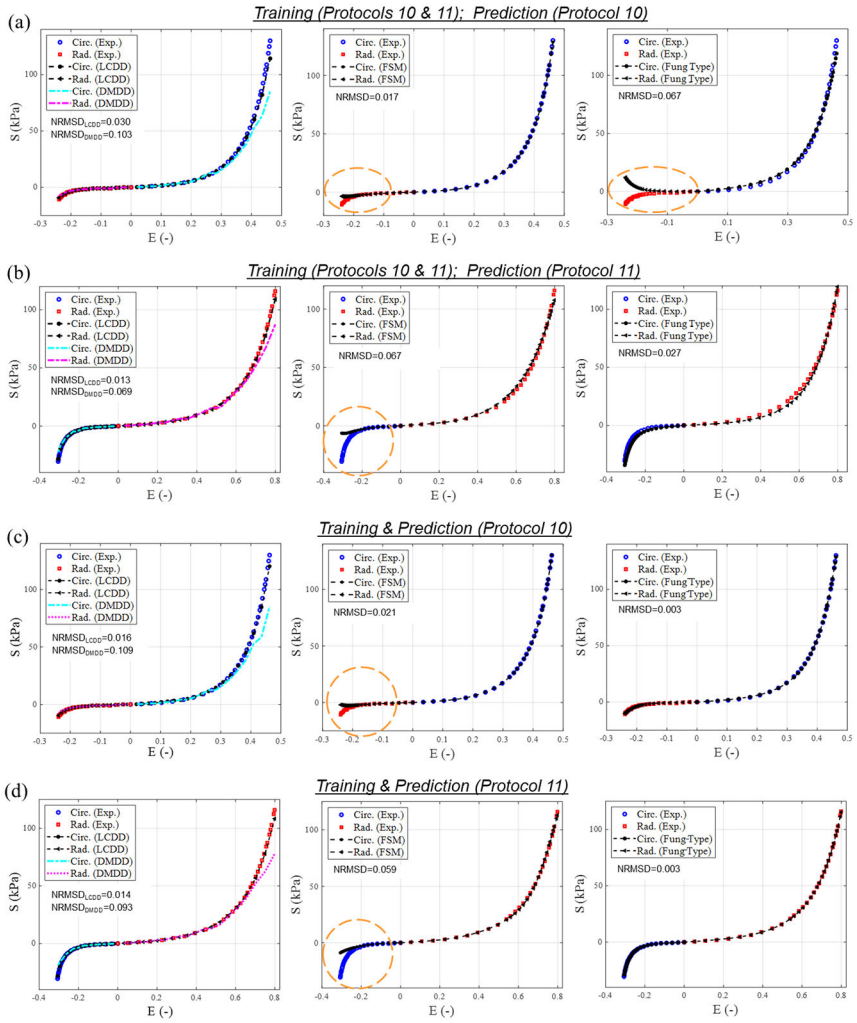

Figure 4.

Comparison of the prediction performance among the proposed LCDD nonlinear solver, the DMDD solver, and the constitutive models with the Fung-type SEDF and the modified full structural model: (a) training using both Protocols 10 & 11 and the prediction of Protocol 10 (*tension in the circumferential direction and compression in the radial direction*), (b) training using Protocols 10 & 11 and the prediction of Protocol 11 (*tension in the radial direction and compression in the circumferential direction*), (c) training of Protocol 10 together with its prediction, and (d) training of Protocol 11 together with its prediction.

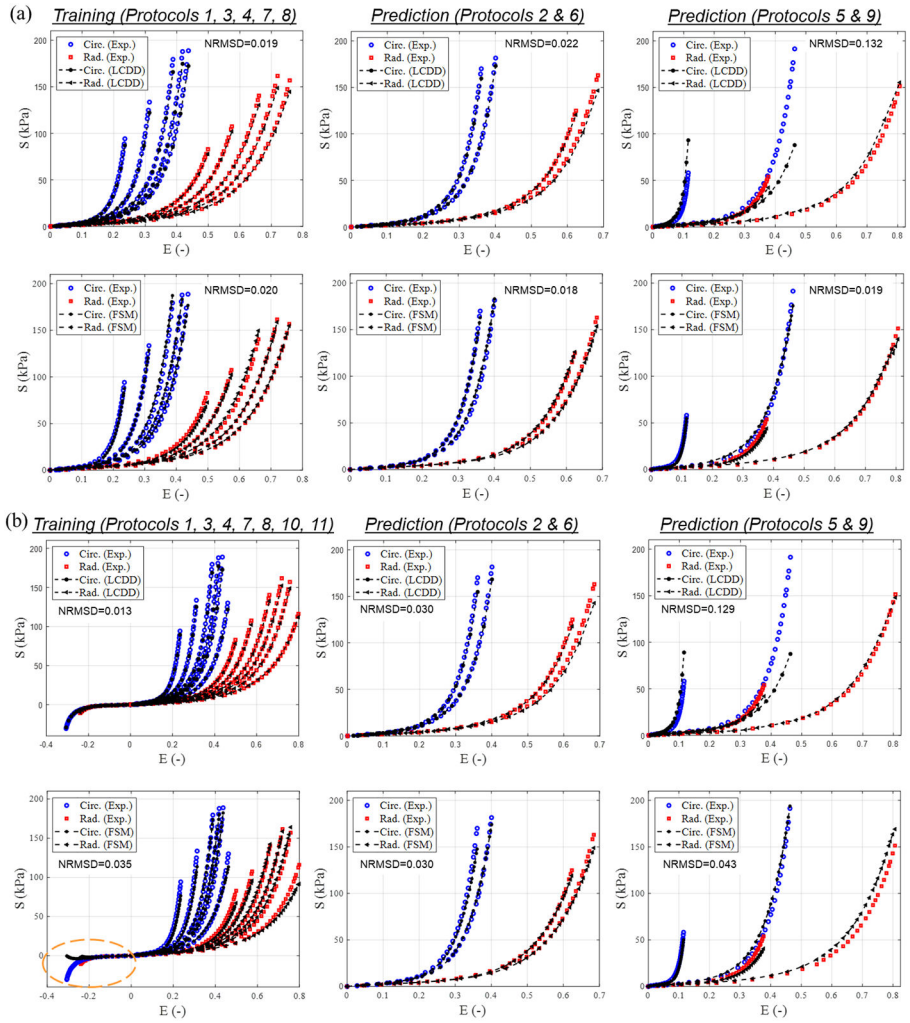

Figure 5.

Comparison of the interpolative and extrapolative predictability between the proposed LCDD nonlinear solver and constitutive modeling with the modified full structural model: (a) training using Protocols 1, 3, 4, 7, and 8 *without* the pure shear protocols together with its predictions of Protocols 2 & 6 (*interpolative*) and Protocols 5 & 9 (*extrapolative*), and (b) training using Protocols 1, 3, 4, 7, and 8 *together with* the two pure shear protocols together with its interpolative and extrapolative predictions.

Table 1.

Eleven protocols of the conducted biaxial mechanical testing with the experimentally-quantified tissue stretches of a representative MVPL specimen and their equivalent displacements used in the data-driven computations (see Fig. 2c-e).

Protocol ID	Testing Protocol	λ_{Circ}	λ_{Rad}	u_x (mm)	u_y (mm)
1	Biaxial Tension T_{Circ}:T_{Rad} = 1:1	1.333	1.525	2.498	3.938
2	Biaxial Tension T_{Circ}:T_{Rad} = 1:0.8	1.342	1.499	2.564	3.744
3	Biaxial Tension T_{Circ}:T_{Rad} = 1:0.6	1.355	1.466	2.662	3.498
4	Biaxial Tension T_{Circ}:T_{Rad} = 1:0.4	1.369	1.415	2.770	3.110
5	Biaxial Tension T_{Circ}:T_{Rad} = 1:0.2	1.388	1.326	2.913	2.442
6	Biaxial Tension T_{Circ}:T_{Rad} = 0.8:1	1.313	1.541	2.344	4.055
7	Biaxial Tension T_{Circ}:T_{Rad} = 0.6:1	1.275	1.562	2.064	4.215
8	Biaxial Tension T_{Circ}:T_{Rad} = 0.4:1	1.213	1.588	1.596	4.409
9	Biaxial Tension T_{Circ}:T_{Rad} = 0.2:1	1.109	1.618	0.820	4.635
10	Pure Shear in x (x: tension, y: compression)	1.387	0.721	2.903	−2.093
11	Pure Shear in y (x: compression, y: tension)	0.620	1.612	−2.847	4.590

Note that the mounting size of the MVPL tissue specimen is 7.5x7.5 mm.